Two-link swimming using buoyant orientation

L. J. Burton,[1,a)] R. L. Hatton,[2] H. Choset,[2] and A. E. Hosoi[1]
[1]*Massachusetts Institute of Technology, Cambridge, Massachusetts 02139, USA*
[2]*Carnegie Mellon University, Pittsburgh, Pennsylvania 15213, USA*

The *scallop theorem* posits that a two-link system immersed in a fluid at low Reynolds number cannot achieve any net translation via cyclic changes in its hinge angle. Here, we propose an approach to "breaking" this theorem, based on a static separation between the centers of mass and buoyancy in a net neutrally buoyant system. This separation gives the system a natural equilibrium orientation, allowing it to passively reorient without changing shape. © *2010 American Institute of Physics*. [doi:10.1063/1.3481785]

A growing interest in natural and artificial microswimming has led to a variety of recent studies that addresses the unique challenges associated with swimming at small scales. A microswimmer's inertia is negligible compared to the effects of viscosity of the surrounding fluid (i.e., the Reynolds number is small); as such, these swimmers must employ strokes that do not depend on momentum to achieve a net translation. A well recognized consequence of this constraint is Purcell's *scallop theorem*,[1] which states that in low Reynolds number flows, a system with a single internal degree of freedom cannot locomote. This theorem has led to several investigations of minimal swimming that examine the smallest increase in complexity needed to generate a system capable of locomotion.

Many of these investigations have focused on breaking the symmetry of the swimmer by adding internal degrees of freedom, either through actively controlled joints,[2] or passive flexible members.[3] Other approaches have been to change the environment by using temporally and/or spatially varying magnetic fields to actuate or pull a passive swimmer,[4] posing the swimming problem in a viscoelastic fluid,[5] or adding inertia to the body only, so that the inertia of the fluid is still negligible.[6]

In this letter, we show that adding a static separation of the system's centers of mass and buoyancy gives the neutrally buoyant system an equilibrium orientation to which it passively returns. As the swimmer deforms its body, it changes the orientation of the line between its centers of mass and buoyancy. This rotation is countered by gravity that acts to restore the swimmer to its equilibrium orientation with the center of buoyancy above the center of mass, an effect observed in live microorganisms.[7] If the time scales for these two effects are comparable, the swimmer is supported by a new model incorporating low Reynolds number fluid dynamics with locomotion analysis techniques adopted from the robotics community. This approach allows for both simple computation and concise, intuitive visualization.

The two-link swimmer model is illustrated in Fig. 1. Both links are assumed to be rigid and slender with length L and radius R. The swimmer is neutrally buoyant. The *drag arm* is massless, while the *buoyant arm* has mass m. This arm's mass is distributed such that the center of buoyancy is a distance l further than the center of mass from the hinge, producing a buoyant moment on that arm. The system's shape is described by the angle α between the buoyant arm and the drag arm; its position in the inertial reference frame is given by (x, y), the location of the hinge axis, and the orientation θ of the medial line bisecting the swimmer, measured from the vertical.

If the centers of gravity and buoyancy were collocated, opening or closing the hinge would only serve to propel the swimmer back and forth along its medial line. Separating the centers gives the system a tendency to return the buoyant arm to a vertical configuration and thus allows it to passively reorient between the opening and closing motions, producing a net displacement. The attractive feature of this mechanism lies in its simplicity that manifests as a passive response to a stationary field. Note that the swimmer can translate upwards against gravity.

As noted above, at the low Reynolds numbers we are considering, viscous drag forces dominate and inertial effects are negligible. This has several key consequences we can exploit to represent the equations of motion in a concise manner. First, the net force on the swimmer is zero. Second, the drag forces acting on the system are linear in the velocities of the links, which are in turn linear in the system's shape and position velocities and independent of the location (but not the orientation) of the system in the inertial frame. Together, these properties form the force-balance equation
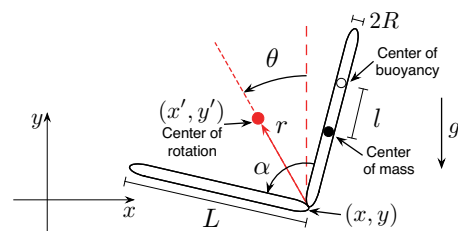

FIG. 1. (Color online) Schematic of the neutrally buoyant, two-link swimmer with centers of mass and buoyancy separated by a distance l.

a)Electronic mail: lisab@mit.edu.

$$\begin{bmatrix} F_g^x & F_g^y & F_g^\theta \end{bmatrix}^T = -\begin{bmatrix} F_d^x & F_d^y & F_d^\theta \end{bmatrix}^T = \beta^{3\times4}\begin{bmatrix} \dot{x} & \dot{y} & \dot{\theta} & \dot{\alpha} \end{bmatrix}^T, \tag{1}$$

where F_g denotes the net generalized forces applied by gravity, F_d denotes the drag forces that balance these external forces, and $\beta(\alpha,\theta)$ is a linear map relating these forces to the system velocities.

Separating β into two sub-blocks as $\beta=[\beta_1^{3\times3} \ \beta_2^{3\times1}]$ allows us to rearrange Eq. (1) into a form

$$\dot{x} = \begin{bmatrix} \dot{x} & \dot{y} & \dot{\theta} \end{bmatrix}^T = \mathcal{A}(\alpha,\theta)\dot{\alpha} + \mathcal{C}(\alpha,\theta), \tag{2}$$

where $\mathcal{A}(\alpha,\theta)=\beta_1^{-1}\beta_2$ linearly maps an input shape velocity $\dot{\alpha}$ to the resultant $\dot{x}$ position velocities, and $\mathcal{C}(\alpha,\theta)=\beta_1^{-1}F_g$ is an additional position velocity induced by the buoyant forces. Equation (2) is an example of a *reconstruction equation*[8] similar to those presented for three-link systems in Melli *et al.*,[9] Hatton and Choset,[10] and Kanso *et al.*[11] From these and related works, we draw the term *local connection* to describe $\mathcal{A}$.

Our model has two notable differences from those described in the referenced works. First, we now include the *buoyant function* $\mathcal{C}$, which has not appeared previously and whose closest antecedent is the momentum terms included in works such as Ostrowski and Burdick[12] and Shammas *et al.*[13] Second, we have chosen to express the reconstruction equation in terms of inertial-frame velocities, rather than the body-frame velocities used in the previous work. This choice, prompted by the dependence of $\mathcal{C}$ on θ regardless of the frame chosen, avoids any problems posed by integrating in a body frame to find the swimmer's trajectory.[10] Unfortunately, it also results in the unactuated orientation θ appearing on the right-hand side of the reconstruction equation, preventing the direct specification of the right-hand side input trajectories. In this letter, we address these problems with a combination of analytical and numerical limit cycle in the (α,θ) phase space of the swimmer.

As a prelude to this limit cycle analysis, it is useful to briefly review the physics of low Reynolds number swimming that give rise to Eq. (2), and to expand the techniques we have previously developed for visualizing locomoting system dynamics[10] to encompass the present system. In general, the β matrix that produces the drag forces in Eq. (1) can be found by solving Stokes's equations around the links. For this analysis, we assume a small aspect ratio, $R/L \ll 1$, and use the resistive-force theory[14] to approximate the drag forces acting on the links. With this model, the lateral and longitudinal drag forces on each link are proportional to the lateral and longitudinal velocities by drag coefficients κ and $\kappa/2$, respectively.

Standard kinematics techniques[15] relate these velocities to the generalized coordinate velocities in Eq. (1) and also provide the rotations to bring them into a common frame for summation into F_d^x and F_d^y. The drag moments are handled similarly, with the note that F_d^θ is the sum not only of the rotational drag moments but also of the moments resulting from the drag forces acting normal to the link. Resistive-force theory does not capture long-range hydrodynamic interactions between the links or any viscous effects that arise

from bringing the links close to each other, but it is useful for this initial investigation as it allows an analytical representation of the drag forces. Including the lowest-order long-range interactions by using slender-body theory[16] is straightforward and will be considered in future work.

The gravitationally generated forces in Eq. (1) are similarly derived from the system geometry. Because the swimmer is neutrally buoyant, F_g^x and F_g^y are zero. The moment exerted on the system by the separated gravitational and buoyant forces is given by $F_g^\theta = mgl\sin(\alpha/2-\theta)$.

Rescaling the equations of motion, we take the characteristic translational velocity of the system as ωL and the characteristic angular velocity as ω, where ω^{-1} is the characteristic time scale of our input "flapping" motions corresponding to a dimensionless time $\hat{t}=\omega t$. Combining these velocities in a dimensionless parameter $\gamma=(mgl)/(\kappa\omega L^2)$, corresponding to the ratio of gravitational and drag forces, Eq. (2) becomes

$$\begin{bmatrix} \hat{x} \\ \hat{y} \\ \hat{\theta} \end{bmatrix} = \frac{\sin\dfrac{\alpha}{2}}{3-\cos\alpha}\begin{bmatrix} -\sin\theta \\ \cos\theta \\ 0 \end{bmatrix}\hat{\dot{\alpha}}$$
$$+ \frac{3\gamma}{3-\cos\alpha}\begin{bmatrix} [\sin(\alpha-\theta)-\sin\theta]\cos\theta \\ [\sin(\alpha-\theta)-\sin\theta]\sin\theta \\ (3+\cos\alpha)\sin\left(\dfrac{\alpha}{2}-\theta\right) \end{bmatrix}, \tag{3}$$

revealing the characteristic trajectory of the system to be a function only of the chosen flapping motion $\hat{\alpha}$ and the parameter γ. The dimensionless parameter γ has a second interpretation, relating the settling time of the swimmer to the characteristic time scale of flapping.

Our choice of the medial line as the swimmer's orientation has a convenient effect on the form of Eq. (3). In these coordinates, the two links open and close symmetrically around the orientation line, which consequently does not rotate in response to changes in the hinge angle; this symmetry leads to the third row of $\mathcal{A}$ being zero. The swimmer also has a second, less intuitive symmetry that allows further reduction of the reconstruction equation. Because the gravitational forces are a pure moment applied to the system, they induce a rigid rotation of the swimmer about a shape-dependent center of rotation defined by the interactions of the drag forces on the links. By symmetry, this center of rotation is on the medial line, and we can most easily calculate its distance r from the hinge by recognizing that the moment-induced motion of the hinge is along an arc around the center of rotation, and thus

$$\hat{r} = r/L = -\mathcal{C}_x/(\mathcal{C}_\theta\cos\theta) = 2\cos(\alpha/2)/(3+\cos\alpha). \tag{4}$$

Changing the reference location of the system from the hinge to the center of rotation by selecting $(\hat{x}',\hat{y}')=(\hat{x}-\hat{r}\sin\theta,\hat{y}+\hat{r}\cos\theta)$ is a form of optimal coordinate choice,[10] and has the effect of reducing $\mathcal{C}_x$ and $\mathcal{C}_y$ to zero, producing a new reconstruction equation,
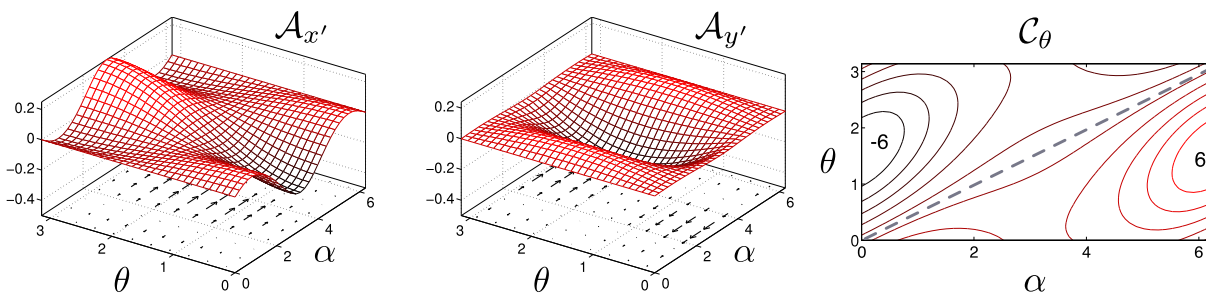
FIG. 2. (Color online) Visualization of the components of the equations of motion in Eq. (5) for $\gamma=1$. Left: connection vector fields for $\mathcal{A}_{x',y'}(\alpha,\theta)$, along with their curls, capture the contribution to translation from changes in shape. Right: $\mathcal{C}_\theta(\alpha,\theta)$, represents the contribution to rotation from the buoyant moment. The dashed line indicates the equilibrium orientation.

$$\begin{bmatrix} \hat{x}' \\ \hat{y}' \\ \hat{\theta} \end{bmatrix} = \begin{bmatrix} \mathcal{A}_{x'}\hat{\alpha} \\ \mathcal{A}_{y'}\hat{\alpha} \\ \mathcal{C}_\theta \end{bmatrix} = \begin{bmatrix} -\sin\theta\left(\dfrac{\sin(\alpha/2)}{3-\cos\alpha}+\dfrac{d\hat{r}}{d\alpha}\right)\hat{\alpha} \\ \cos\theta\left(\dfrac{\sin(\alpha/2)}{3-\cos\alpha}+\dfrac{d\hat{r}}{d\alpha}\right)\hat{\alpha} \\ \dfrac{3\gamma}{3-\cos\alpha}(3+\cos\alpha)\sin\left(\dfrac{\alpha}{2}-\theta\right) \end{bmatrix}, \quad (5)$$

in which the translational velocity is generated entirely by the local connection, and the rotational velocity is dictated exclusively by the buoyant terms.

The components of the reconstruction equation in Eq. (5) are displayed graphically for $\gamma=1$ in Fig. 2. The two leftmost plots represent the rows of the local connection $(\mathcal{A}_{x'},\mathcal{A}_{y'})$ using the *connection vector field* metaphor previously employed for locomoting systems.[10] The dot products of an input $\hat{\alpha}$ with the vector fields produce the contribution of the shape velocity to the position velocity, as per the first line in Eq. (5). The curls of the rows of $\mathcal{A}$ capture all the information about the net contribution of this opening and closing action over a full cycle. By Stokes's theorem, line integrals along closed loops, which represent cyclical body deformations, are equal to the area integrals of the fields' curls over the region enclosed by the loops. At the right of the figure, the contour plot illustrates $\mathcal{C}_\theta$ and can be interpreted as the prescribed rotational velocity imposed on the system by the buoyant moment.

The chief weakness of this form of the reconstruction equation is the presence of θ as an unactuated configuration component on the right-hand side. The first step in analyzing strokes for the swimmer, then, is to identify the limit-cycle behavior of θ in response to given cyclic α inputs; once this behavior is found, the translatory component of the motion can be found by evaluating Eq. (5) for the corresponding (α,θ) trajectory.

To find this limit cycle, we take advantage of the structure of Eq. (5), specifically the property that the orientation trajectory is entirely defined by the buoyant moment, $\hat{\theta}(\hat{t})=\mathcal{C}_\theta(\alpha,\theta)$. For strokes covering large ranges of α, $\mathcal{C}_\theta$ is sufficiently nonlinear that we take recourse to numerical methods when solving for θ. For small strokes, however, we can find an analytical expression for this trajectory by linearizing the buoyant moment as $\mathcal{C}_\theta=k[\theta_n(\alpha)-\theta]$, where $k=6\gamma$ acts as a linear restoring spring driving θ toward its equilibrium value of $\theta_n=\alpha/2$, indicated by the dashed line in the $\mathcal{C}_\theta$ plot

in Fig. 2. This linearization then allows $\hat{\theta}(\hat{t})$ to be rewritten as the ordinary differential equation

$$\hat{\dot{\theta}}(\hat{t})+k\theta(\hat{t})=k\alpha(\hat{t})/2. \quad (6)$$

We now select an input shape trajectory $\alpha(\hat{t})=\alpha_0/2+\alpha_0/2\sin(\hat{t})$, i.e., a sinusoidal opening and closing motion with frequency determined by the characteristic time scale. Substituting this input into Eq. (6) and solving the differential equation produces the limit cycle for the θ trajectory corresponding to this input,

$$\theta(\hat{t})=\frac{\alpha_0}{4}+\frac{\alpha_0 k}{4(1+k^2)}[k\sin(\hat{t})-\cos(\hat{t})], \quad (7)$$

which depends only on the amplitude of the input α_0 and the time scale parameter γ.

Together, $\alpha(\hat{t})$ and Eq. (7) form elliptical trajectories in the (α,θ) space, sheared such that the θ components of the tangent vectors are zero where the trajectory crosses the equilibrium line, enclosing areas $a=(\pi\alpha_0^2 k)/[8(1+k^2)]$ in the (α,θ) plane. Comparing these ellipses to exact integrals of Eq. (3) for the input in $\alpha(\hat{t})$, as in Fig. 3, shows the approximate trajectories to be a reasonable representation of the system behavior for input amplitudes of $\alpha_0<1.5$. At larger amplitudes, the nonlinearities in $\mathcal{C}_\theta$ start to play a significant role with their first effect being a reduction in the restoring force below the equilibrium line. This reduction pulls the α_{max} tips of the trajectories down to lower values of θ.

With the (α,θ) limit cycles in hand, we can now consider the efficiencies $\mathcal{E}$ of strokes at different amplitudes and frequencies, which we take as the ratio of the power required to pull the swimmer at its nondimensionalized mean speed $\hat{s}$ (relative to the flapping frequency) to the time averaged me-
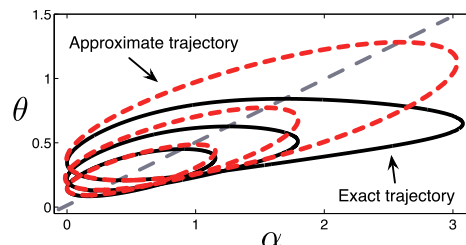

FIG. 3. (Color online) Comparison of exact stroke limit cycles with the shape predicted by the linearized model, for $\gamma=1/6$ and $1.2<\alpha_0<3.1$. Dashed lines indicate trajectories from the linearized solutions, solid lines indicate exact trajectories.
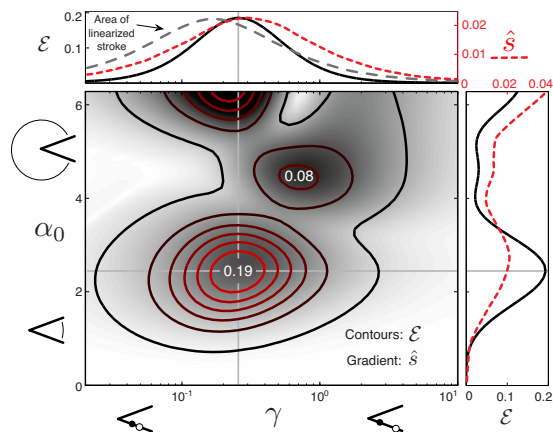
FIG. 4. (Color online) Contours: efficiency $\mathcal{E}$ (in percent) of the system as a function of stroke amplitude α_0 and time scale parameter γ. Gradient background: dimensionless mean speed $\hat{s}$. Top and side panels: qualitative comparison of the efficiency with the mean speed $\hat{s}$ of the system relative to the flapping frequency. The mean speed corresponds to the area integral of the curl functions over the region of the (α, θ) space enclosed by the stroke; the top panel additionally presents the dependence of the enclosed area on γ for the linearized stroke.

chanical power applied through the hinge to generate the system's motion.[17] Calculating this efficiency numerically is straightforward, generating the contour surface in Fig. 4. Note that $\hat{s}$ can be calculated either by integrating Eq. (5) or by using the area integrals of the curl functions over the regions enclosed by the strokes to find the net displacement per cycle. The dominating features of this plot are the three peaks in efficiency for γ values between 10^{-1} and 10^0, when the time scales of flapping and settling are comparable. Mean speed, represented as a gradient surface behind the contours in Fig. 4, is closely correlated with the efficiency. This correspondence is explained by recognizing that $\hat{s}$ can alternately be taken as a measure of displacement per stroke, and thus as a kind of efficiency measure in its own right.

Independently, these peaks highlight the best choices of input amplitude and frequency to generate efficient motion. Combining them with information from the curl functions in Fig. 2 provides further insight into several key features of the system dynamics. Physically, the curl functions measure the extent to which reorienting the system breaks the time symmetry. By observing the interactions of the strokes with the curl functions, we can elucidate the system behaviors that give rise to the peaks.

Starting at $\alpha_0 = 0$ and moving up the plot, the first peak and its surrounding values represents optimal system behavior for $\alpha_0 < \pi$. For these amplitudes, the optimal γ values are very close to the values that maximize the area a enclosed by the (α, θ) trajectory, as illustrated in the top panel of Fig. 4. Returning to the curl functions in Fig. 2, we see that for small strokes both curl functions are positive-definite, and thus maximizing the area enclosed by the stroke maximizes the net displacement achieved over the control effort. The drift of the optimal efficiency toward larger γ values (i.e., strokes that are slower or settle more quickly) is largely explained by the differences between the true and linearized strokes noted in Fig. 3. Reducing the flapping frequency allows the system more time to reorient itself between opening

and closing during the part of the cycle that passes through the low-magnitude region of $\mathcal{C}_\theta$, thus reducing the pinching effect on the larger trajectories.

The second peak's origins lie in the dependence of the curl functions on α and θ. As the amplitude increases, the enclosed regions of the curl function are no longer positive-definite. The newly added negative regions (especially present for the y component) first cancel out the positive contributions, causing a dip in efficiency, and then grow to dominate the solution at the second peak. Strokes near this peak spend the majority of their cycle in the low-magnitude region of $\mathcal{C}_\theta$, pushing the peak's γ value significantly above the optimum for the linearized strokes.

Finally, the third peak reflects a similar dip and increase in the area integral magnitudes, with very large strokes enclosing a significant negative region of the y curl function. This final increase in amplitude also places the stroke back in larger-magnitude regions of $\mathcal{C}_\theta$, pulling the peak's maximum efficiency back down to lower values of γ (i.e., strokes that are faster or settle more slowly). As compared to the first peak, strokes near this peak have greater displacement over each cycle (and thus a greater mean speed $\hat{s}$), but this increased displacement is not enough to offset the increased control effort, leaving the first peak as representing the most efficient motion.

[1]E. Purcell, "Life at low Reynolds number," Am. J. Phys. **45**, 3 (1977).
[2]A. Najafi and R. Golestanian, "Propulsion at low Reynolds number," J. Phys.: Condens. Matter **17**, S1203 (2005).
[3]T. Yu, E. Lauga, and A. Hosoi, "Experimental investigations of elastic tail propulsion at low Reynolds number," Phys. Fluids **18**, 091701 (2006).
[4]R. Dreyfus, J. Baudry, M. Roper, M. Fermigier, H. Stone, and J. Bibette, "Microscopic artificial swimmers," Nature (London) **437**, 862 (2005).
[5]H. Fu, T. Powers, and C. Wolgemuth, "Theory of swimming filaments in viscoelastic media," Phys. Rev. Lett. **99**, 258101 (2007).
[6]D. Gonzalez-Rodriguez and E. Lauga, "Reciprocal locomotion of dense swimmers in Stokes flow," J. Phys.: Condens. Matter **21**, 204103 (2009).
[7]T. Pedley and J. Kessler, "Hydrodynamic phenomena in suspensions of swimming microorganisms," Annu. Rev. Fluid Mech. **24**, 313 (1992).
[8]A. M. Bloch, P. Crouch, J. Baillieul, and J. Marsden, *Nonholonomic Mechanics and Control* (Springer, New York, 2003).
[9]J. B. Melli, C. W. Rowley, and D. S. Rufat, "Motion planning for an articulated body in a perfect planar fluid," SIAM J. Appl. Dyn. Syst. **5**, 650 (2006).
[10]R. L. Hatton and H. Choset, "Optimizing coordinate choice for locomoting systems," *Proceedings of the IEEE International Conference on Robotics and Automation in Anchorage*, AK (IEEE, Piscataway, 2010).
[11]E. Kanso, J. Marsden, C. Rowley, and J. Melli-Huber, "Locomotion of articulated bodies in a perfect fluid," J. Nonlinear Sci. **15**, 255 (2005).
[12]J. Ostrowski and J. Burdick, "The mechanics and control of undulatory locomotion," Int. J. Robot. Res. **17**, 683 (1998).
[13]E. A. Shammas, H. Choset, and A. A. Rizzi, "Towards a unified approach to motion planning for dynamic underactuated mechanical systems with non-holonomic constraints," Int. J. Robot. Res. **26**, 1075 (2007).
[14]J. Gray and G. Hancock, "The propulation of sea-urchin spermatozoa," J. Exp. Biol. **32**, 802 (1955).
[15]R. Murray, Z. Li, and S. Sastry, *A Mathematical Introduction to Robotic Manipulation* (CRC, Boca Raton, FL 1994).
[16]R. Cox, "The motion of long slender bodies in a viscous fluid. Part 1. General theory," J. Fluid Mech. **44**, 791 (1970).
[17]L. Becker, S. Koehler, and H. Stone, "On self-propulsion of micromachines at low Reynolds number: Purcell's three-link swimmer," J. Fluid Mech. **490**, 15 (2003).